The Intrinsic Shapes of Low Surface Brightness Galaxies (LSBGs)

Kado-Fong, Erin; Petrescu, Mihai; Mohammad, Majid; Greco, Johnny; Greene, Jenny E.; Adams, Elizabeth A. K.; Huang, Song; Leisman, Lukas; Munshi, Ferah; Tanoglidis, Dimitrios

IMPORTANT NOTE: You are advised to consult the publisher's version (publisher's PDF) if you wish to cite from it. Please check the document version below.

Document Version
Publisher's PDF, also known as Version of record

Link to publication in University of Groningen/UMCG research database

Citation for published version (APA):
Kado-Fong, E., Petrescu, M., Mohammad, M., Greco, J., Greene, J. E., Adams, E. A. K., Huang, S., Leisman, L., Munshi, F., Tanoglidis, D., & Van Nest, J. (2021). The Intrinsic Shapes of Low Surface Brightness Galaxies (LSBGs): A Discriminant of LSBG Galaxy Formation Mechanisms. *The Astrophysical Journal*, *920*, [72]. https://doi.org/10.3847/1538-4357/ac15f0

CrossMark

The Intrinsic Shapes of Low Surface Brightness Galaxies (LSBGs): A Discriminant of LSBG Galaxy Formation Mechanisms

Erin Kado-Fong[1] , Mihai Petrescu[2,3], Majid Mohammad[4] , Johnny Greco[3,11], Jenny E. Greene[1] ,
Elizabeth A. K. Adams[5,6] , Song Huang[1] , Lukas Leisman[7] , Ferah Munshi[8] , Dimitrios Tanoglidis[9,10], and Jordan Van Nest[8]

[1] Department of Astrophysical Sciences, Princeton University, 4 Ivy Lane, Princeton, NJ 08544, USA; kadofong@princeton.edu
[2] Department of Physics, The Ohio State University, 191 West Woodruff Avenue, Columbus OH 43210, USA
[3] Center for Cosmology and AstroParticle Physics (CCAPP), The Ohio State University, Columbus, OH 43210, USA
[4] Department of Physics, Colorado School of Mines, 1523 Illinois Street, Golden, CO 80401, USA
[5] ASTRON, the Netherlands Institute for Radio Astronomy, Oude Hoogeveensedijk 4,7991 PD Dwingeloo, The Netherlands
[6] Kapteyn Astronomical Institute, PO Box 800, 9700AV Groningen, The Netherlands
[7] Department of Physics and Astronomy, Valparaiso University, 1610 Campus Drive East, Valparaiso, IN 46383, USA
[8] Department of Physics and Astronomy, University of Oklahoma, 440 West Brooks Street, Norman, OK 73019, USA
[9] Department of Astronomy and Astrophysics, University of Chicago, Chicago, IL 60637, USA
[10] Kavli Institute for Cosmological Physics, University of Chicago, Chicago, IL 60637, USA

Abstract

We use the low surface brightness galaxy (LSBG) samples created from the Hyper Suprime-Cam Subaru Strategic Program (781 galaxies), the Dark Energy Survey (20977 galaxies), and the Legacy Survey (selected via H I detection in the Arecibo Legacy Fast ALFA Survey, 188 galaxies) to infer the intrinsic shape distribution of the LSBG population. To take into account the effect of the surface brightness cuts employed when constructing LSBG samples, we simultaneously model both the projected ellipticity and the apparent surface brightness in our shape inference. We find that the LSBG samples are well characterized by oblate spheroids, with no significant difference between red and blue LSBGs. This inferred shape distribution is in good agreement with similar inferences made for ultra-diffuse cluster galaxy samples, indicating that environment does not play a key role in determining the intrinsic shape of LSBGs. We also find some evidence that LSBGs are more thickened than similarly massive high surface brightness dwarfs. We compare our results to intrinsic shape measures from contemporary cosmological simulations, and find that the observed LSBG intrinsic shapes place considerable constraints on the formation path of such galaxies. In particular, LSBG production via the migration of star formation to large radii produces intrinsic shapes in good agreement with our observational findings.

Unified Astronomy Thesaurus concepts: Low surface brightness galaxies (940); Dwarf galaxies (416);
Observational astronomy (1145); Astronomical methods (1043); Galaxy structure (622)

1. Introduction

Low surface brightness galaxies, or LSBGs, are an observationally defined galaxy population characterized by a low average surface brightness and large on-sky sizes (e.g., $\langle\mu\rangle_{R_{\rm eff}} > 24.3$ mag arcsec^{-2} and $R_{\rm eff} > 2.5''$ (Greco et al. 2018; Tanoglidis et al. 2021), though specific surface brightness and size cuts vary; ultra-diffuse galaxies (UDGs) are LSBGs with large physical effective radii (e.g., $R_{\rm eff} > 1.5$ kpc, van Dokkum et al. 2015—UDG identification thus requires a distance measurement). The origin and physical properties of this extreme tail of the dwarf population is still a matter of debate—the formation path of LSBGs and their relationship with the general galaxy population has been a topic of sustained interest since their discovery (Sandage & Binggeli 1984; McGaugh et al. 1995; Dalcanton et al. 1997).

Present day simulations have proposed several pathways for the formation of LSBGs and UDGs. It has been proposed that UDGs populate the high-spin tail of dwarf-mass dark matter halos (Amorisco & Loeb 2016; Rong et al. 2017; Liao et al. 2019), are formed via vigorous star formation feedback and outflows (Di Cintio et al. 2017; Chan et al. 2018; Jiang et al. 2019), are formed via effects induced by high-density environments (Jiang et al. 2019; Tremmel et al. 2020), or are the product of early major mergers that trigger the radial migration of star formation

(Wright et al. 2021). Given the significant array of formation scenarios for this class of galaxies, it is of interest to identify observable quantities that may discriminate between the proposed formation mechanisms.

The current generation of deep wide-field surveys have enabled a new generation of systematic studies of thousands of LSBGs over a range of environments (Danieli et al. 2018; Greco et al. 2018; Tanoglidis et al. 2021). However, due to the uncertainty in the distances of LSBG samples, much of the work on the inherent physical properties of these LSBGs has been focused on the UDG populations in groups and clusters wherein the cluster distance may be assumed (van Dokkum et al. 2015; Martínez-Delgado et al. 2016; van der Burg et al. 2016; Yagi et al. 2016; Lee et al. 2017; Román & Trujillo 2017a, 2017b; Danieli & van Dokkum 2019; Mancera Piña et al. 2019a; Román et al. 2019; Rong et al. 2020; Zaritsky et al. 2019; Barbosa et al. 2020; Prole et al. 2021).

The intrinsic, three-dimensional shapes of galaxies provide key insights into the formation and evolution of galaxy structure (see, e.g., Padilla & Strauss 2008; Sánchez-Janssen et al. 2010; Costantin et al. 2018; Méndez-Abreu et al. 2018; Kado-Fong et al. 2020b; Carlsten et al. 2021). Indeed, the morphology and intrinsic shape distribution of LSBGs are key properties that may be explored, even when individual distances are not known. For *normal* high surface brightness (HSB) galaxies, the three-dimensional shape of a galaxy population changes starkly as a function of both mass and color, producing the familiar color-morphology bimodality (see,
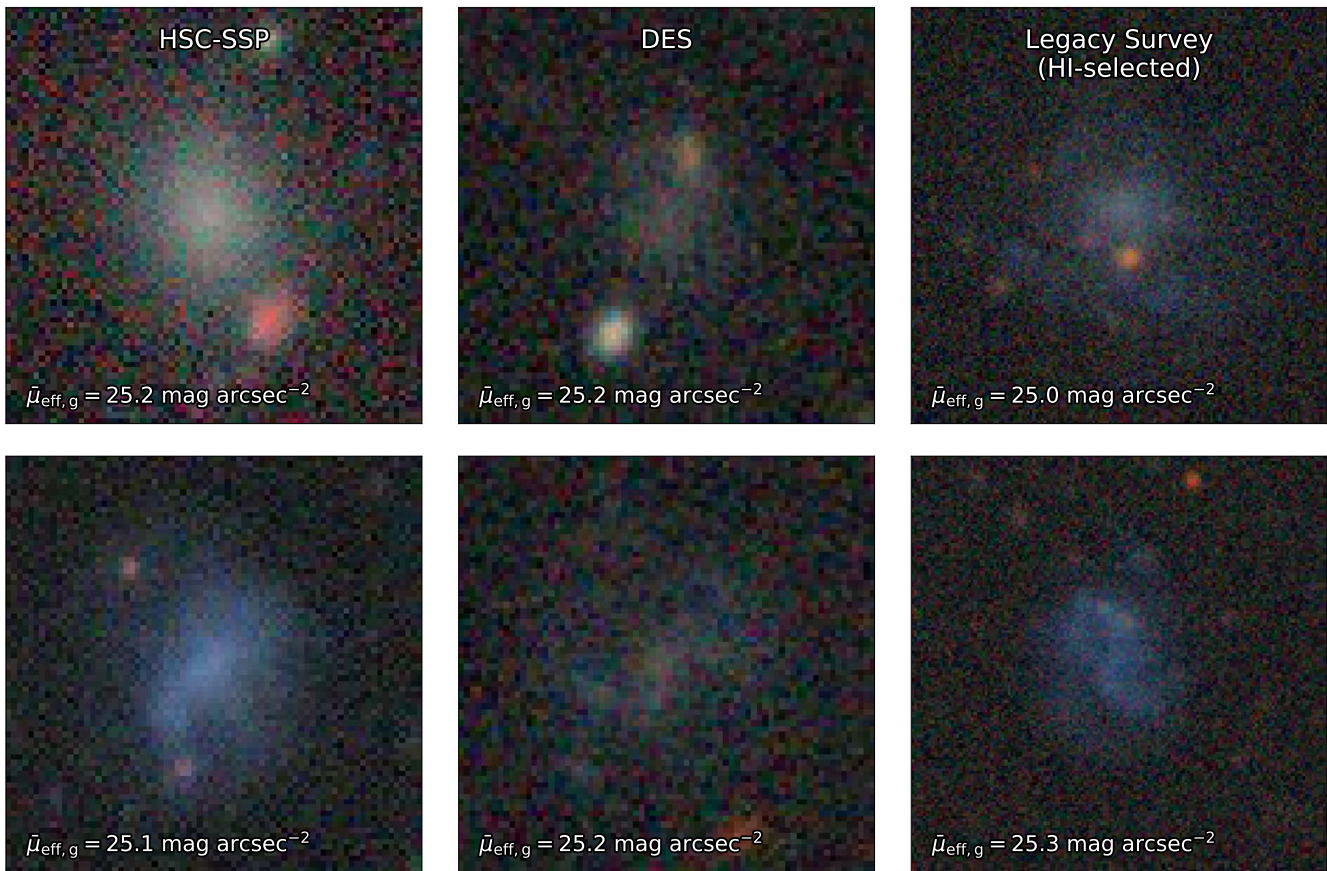
Figure 1. Example grz RGB cutouts from the three imaging sets considered in this work. The top row shows an example from the red end of the sample $((g - r) > \langle(g - r)\rangle_{75}$, where $\langle\rangle_{XX}$ indicates the XXth percentile), while the bottom shows an example from the blue end $((g - r) < \langle(g - r)\rangle_{25})$. Note that because the Legacy Survey UDG sample was originally selected to have H I, the red end of the distribution is still relatively blue in absolute terms. Each example in the figure is chosen to have approximately the same mean effective g-band surface brightness of $\langle\mu\rangle_{R_{eff}} \sim 25$ mag arcsec^{-2}. The cutouts of the HSC and DES imaging are $20''$ on a side, while the Legacy Survey cutout is $40''$ on a side. The galaxies shown for each sample are (top panel, bottom panel): HSC (LSBG-325, LSBG-211), DES (ID224789651, ID214498053), and Legacy (AGC114754, AGC336397).

e.g., Padilla & Strauss 2008). In the dwarf-mass regime, there is evidence of a transition in stellar intrinsic shape from thick disk to oblate spheroid as a function of stellar mass (Sánchez-Janssen et al. 2010; Kado-Fong et al. 2020b). Studies in nearby groups and clusters suggest that UDGs in high-density environments are generally oblate spheroids, though the impact of the environment itself is difficult to ascertain without an analogous sample in less crowded environments. How the structure of the general LSBG population relates to that of HSB galaxies remains largely unexplored.

In this work we combine three LSBG samples to infer the distribution of three-dimensional shapes of the wide-field selected LSBG population: the sample of Tanoglidis et al. (2021) detected from the Dark Energy Survey (DES), the sample of Greco et al. (2018) detected from the Hyper Suprime-Cam Subaru Strategic Program (HSC-SSP), and the H I-selected sample of Janowiecki et al. (2019) selected from the Arecibo Legacy Fast ALFA (ALFALFA) survey and reprocessed using Legacy Survey imaging. These three samples provide complementary views of the LSBG population. The DES and HSC-SSP samples are constructed using very similar methods, and while the DES sample includes a larger number of galaxies, the HSC-SSP sample is drawn from deeper imaging data. The H I-selected sample, meanwhile, is selected using a markedly different approach and has associated distances to each object. In Section 2, we detail the samples, as well as the collation and homogenization of the DES

and HSC-SSP samples, In Section 3, we extend the methodology of Kado-Fong et al. (2020b) to include the effect of intrinsic shape on both ellipticity and surface brightness and provide an overview of the inference machinery used to determine the three-dimensional shape distribution. We present our main findings for the samples and for color subsets of the DES sample in Section 4, and contextualize our findings with previous observational and theoretical work in Section 5. Throughout this paper we adopt a standard flat Λ cold dark matter model in which $H_0 = 70$ km s^{-1} Mpc^{-1} and $\Omega_m = 0.3$.

2. Sample Construction

In this work we use the LSBG catalogs created by Tanoglidis et al. (2021) and Greco et al. (2018). These catalogs are created using very similar methods, though the surface brightness limit of the DES imaging is significantly brighter than the deeper HSC-SSP imaging. We additionally reanalyze the galaxies of Janowiecki et al. (2019) using imaging from the eighth data release of the Legacy Survey (Dey et al. 2019), both in order to take advantage of the deeper Legacy Survey imaging and to process the H I-selected sample using a method consistent with that of Greco et al. (2018) and Tanoglidis et al. (2021). In Figure 1, we show examples cutouts from each imaging set used in this work. Examples are drawn to span the range of colors represented by the sample, and are chosen to have approximately the same mean effective surface brightness.

For all surface brightnesses in this work we refer to the mean surface brightness within one circularized effective radius, i.e.,

$$\langle\mu\rangle_{R_{\rm eff,circ}} = m(<R_{\rm eff,circ}) - 2.5\log_{10}(\pi R_{\rm eff}^2), \qquad (1)$$

as derived from single Sérsic fits, where $R_{\rm eff,circ}$ refers to the circularized effective radius ($R_{\rm eff,circ} = a\sqrt{b/a}$, where a and b are the observed semimajor and semiminor axes, respectively).

2.1. The HSC-SSP Sample

HSC-SSP is an ongoing wide-field survey conducted on board the 8.2 m Subaru HSC telescope set to cover around 1400 deg^2 to a 5σ point-source depth of $g_{\rm HSC} = 26.6$ mag with a seeing of 0.77″ (Aihara et al. 2019). The exceptional depth and coverage of this survey make it a powerful tool for the discovery of low surface brightness (LSB) structures (see, e.g., Greco et al. 2018; Huang et al. 2018; Kado-Fong et al. 2018; Wang et al. 2019; Kado-Fong et al. 2020a). In this work, we use the catalog of 781 LSBGs found by Greco et al. (2018) in the first ∼200 deg^2 of the survey.

This LSBG sample was constructed using a specialized pipeline detailed in Greco et al. (2018); for the reader's convenience, we summarize the main points of the method here. The main aim of the pipeline is to detect contiguous and extended LSB sources. There are two main contaminants in this goal: LSB structures associated with bright galaxies (i.e., tidal features or extended stellar halos) and faint background galaxies. To remove the former, an iterative thresholding is applied wherein objects with at least 15% of their pixels elevated above 28σ over the global background are discarded from the sample. To remove the latter, each detection is required to contain at least 100 contiguous pixels. Single component Sérsic models are then fit to each remaining source using the software imfit[12] (Erwin 2015) and visually inspected. This visual inspection removes spurious detections due to LSB contaminants; these are most typically galactic cirrus, tidal features from massive galaxies, and wings of bright stars. Finally, each galaxy is required to have an effective radius of $R_{\rm eff} > 2.5″$, a $g_{\rm HSC}$-band mean effective surface brightness (measured within the circularized effective radius) of $24.3 < \langle\mu\rangle_{R_{\rm eff}} < 28.8$ mag arcsec^{-2}, and an ellipticity ($\epsilon = 1 - b/a$, where b/a is the ratio of the semiminor to semimajor axis) of $\epsilon < 0.7$.

The selection function of the Greco et al. (2018) sample has been explored in detail (Greco 2018, Chapter 5) via the injection of mock LSBGs (characterized by single Sérsic profiles) into HSC-SSP imaging. These mock galaxies are processed through the same HSCPIPE (Bosch et al. 2018) data reduction pipeline that was employed for the reduction of the imaging used for the Greco et al. (2018) analysis. These tests in particular explore detection efficiency as a function of angular size, surface brightness, and Sérsic index. They find that the detection efficiency of the Greco et al. (2018) pipeline as a function of surface brightness is largely independent of angular size, though at surface brightnesses below the 80% completeness limit ($\mu_{\rm eff} = 26.5$ mag arcsec^{-2}), detection efficiency is higher for galaxies with larger angular sizes. Similarly, detection efficiency as a function of angular size is independent of Sérsic index for galaxies with angular sizes greater than $R_{\rm eff} \gtrsim 4″$. Detection efficiency is higher for low Sérsic indices below this angular size. We thus conclude that for the purpose of our work, which does not focus on galaxies below this 80% completeness limit, the dependence of detection efficiency on size and Sérsic index should not greatly affect our results. Indeed, we have performed the analysis detailed in this work using both the full Greco et al. (2018) sample and a surface brightness limited sample ($\langle\mu\rangle_{R_{\rm eff}} < 26.5$ mag arcsec^{-2}), and find that our results do not change at statistically significant levels.

2.2. The DES Sample

Though the depth of HSC-SSP allows for the discovery of very faint LSBGs, the restricted area of the Greco et al. (2018) catalog makes the 3D shape inversion problem intractable for subsets of the catalog sample. To overcome this limitation, we will also utilize a sample of 20,977 LSBGs selected from ∼5000 deg^2 in the first 3 yr of DES. The published version of Tanoglidis et al. (2021) contains 23,790 LSBGs with a mean effective surface brightness cut of $\langle\mu\rangle_{R_{\rm eff}} > 24.2$ mag arcsec^{-2}. We use an earlier version of the catalog with a mean effective surface brightness cut of $\langle\mu\rangle_{R_{\rm eff}} > 24.3$ mag arcsec^{-2}, consistent with Greco et al. (2018), as measured by SExtractor. Both versions of the catalog have been made publicly available by the DES team.[13]

The sample construction of the Tanoglidis et al. (2021) sample is, by design, quite similar to that of the Greco et al. (2018) sample. However, there are a number of significant differences, which we will enumerate here for convenience. First, the DES sample selection was performed on the DES Y3 Gold coadd object catalog v2.2 (Sevilla-Noarbe et al. 2021). Second, they employed a support vector machine classifier trained from an initial visual classification in order to remove contaminant objects. Remaining false positives were then removed via visual inspection. Like the Greco et al. (2018) sample, this visual inspection removes common LSB contaminants from the final sample. Finally, the size and average surface brightness cuts were made on the SExtractor measurements, not on the single component Sérsic model fits.

Though a direct measurement of the completeness of this catalog has not yet been made, we can make an empirical estimate using the surface brightness distribution of the Greco et al. (2018) sample, which is drawn from a deeper survey, as a benchmark. In particular, the surface brightness distribution of the red ($g - i > 0.64$) LSBGs in the Greco et al. (2018) sample is consistent with being flat down to their 80% completeness limit in surface brightness. We therefore estimate the 80% completeness limit of the DES LSBG sample to be at the point where the surface brightness distribution of red galaxies in the DES sample diverges significantly from that of the HSC-SSP sample. Because the surface brightness completeness of the HSC sample has been extensively tested via mock injections, we base our completeness estimate of the DES sample on the divergence in surface brightness limit from the HSC sample. The red LSBG surface brightness distribution of the two samples is shown in Figure 2; using this approach, we find a completeness limit of $\langle\mu\rangle_{R_{\rm eff}} \sim 25.75$ mag arcsec^{-2} for the DES LSBG sample.

Though the initial LSBG sample of Tanoglidis et al. (2021) is based on surface brightnesses measured with SExtractor, the final sample selection is made using surface brightness measurements from galfit.

---

[12] https://github.com/perwin/imfit

[13] https://des.ncsa.illinois.edu/releases/other/y3-lsbg
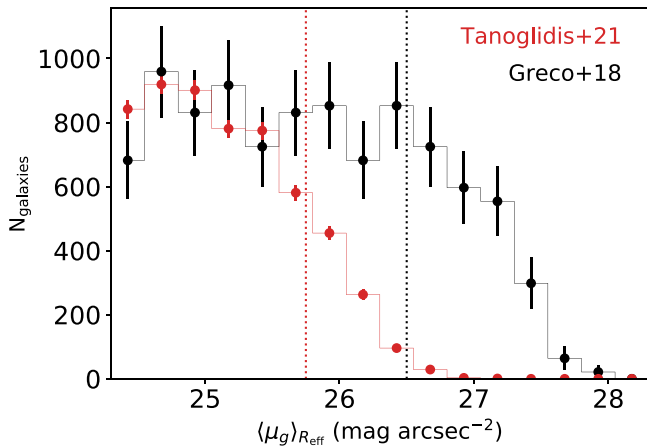
Figure 2. Surface brightness distributions of the red ($(g - i) > 0.64$) galaxies in the DES (Tanoglidis et al. 2021, red) and HSC-SSP (Greco et al. 2018, black) LSBG samples. The $\langle\mu\rangle_{R_{eff}} = 26.5$ mag arcsec^{-2} 80% completeness limit for the HSC-SSP LSBG sample (J. Greco et al., 2021 in preparation) is shown by the dotted black vertical line. We empirically measure the completeness limit of the DES sample as the $\langle\mu\rangle_{R_{eff}}$ at which the surface brightness distribution diverges from that of the deeper HSC-SSP sample.

2.3. The ALFALFA/Legacy Sample

Finally, we include in our analysis the H I-selected UDG sample of Janowiecki et al. (2019). The sample is an environment-blind sample originally selected UDGs in H I from the ALFALFA survey (Giovanelli et al. 2005; Haynes et al. 2011) and measured the optical properties of the associated galaxies using imaging from the Sloan Digital Sky Survey (SDSS; York et al. 2000) using the same methods as Leisman et al. (2017), who selected an analogous sample of isolated H I-bearing UDGs. Because of the relatively shallow depth of SDSS, Leisman et al. (2017) and Janowiecki et al. (2019) assumed an exponential surface brightness distribution and an ellipticity of $\epsilon = 0$. For this work, we use imaging from the deeper Legacy Survey (Dey et al. 2019, point-source 5σ limiting magnitude of $g = 24$) for the 188 galaxies in the Janowiecki et al. (2019) sample covered by Legacy Survey imaging to model the surface brightness distributions as single Sérsic functions where the Sérsic index and ellipticity are allowed to vary.

Using the R_{eff} measurements provided by Janowiecki et al. (2019), we obtained centered cutouts of the galaxies from the Legacy survey's Data Release 8 of size $20R_{eff}$ on a side. The Sérsic fits were carried out using the same methodology as Greco et al. (2018), as summarized in Section 2.1, though we used sep (Barbary 2016) to obtain the initial object segmentation maps. Due to the irregularity of the galaxies and large amount of interfering background sources and/or bright star formation knots, ~40% of the object masks were manually adjusted. Measurements from sep were also used to provide initial size and ellipticity guesses to imfit. The new measurements made for this paper will made be public in a forthcoming work (M. Petrescu et al. 2021 in preparation).

2.4. The Coma Cluster Sample

In order to expand the range of environments probed in this study, we further include the Coma cluster sample of Alabi et al. (2020), who construct a catalog of Coma Cluster galaxies with a specific focus on extending the set of known LSBGs in

the Coma Cluster. They performed an initial selection using SEXtractor and refined the sample via visual inspection and structural parameter inference via GALFIT. We use the catalog measurements of Alabi et al. (2020) for this analysis, and thus caution that the methods used for the structural measurements of this sample differ significantly than those used for the HSC-SSP, DES, and H I-selected samples, which are all based on the methodology of Greco et al. (2018). We provide an abbreviated description of the catalog construction method of Alabi et al. (2020) for completeness. First, they perform an initial object detection using SEXtractor to remove stars and compact (FWHM $\lesssim 0.5$ kpc) objects. Next, they use a cut in the R-band magnitude-surface brightness plane to identify a sample of galaxies to model. All the remaining galaxies are modeled with one-component Sérsic profiles using GALFIT (Peng et al. 2010). Finally, the Sérsic fits are evaluated, and they remove high ($n > 2$) Sérsic index galaxies that are redder than 1σ from the red sequence at the distance of Coma. We use the structural parameters measured from a single Sérsic fit to the Subaru Suprime-Cam R-band data of Alabi et al. (2020). We consider only galaxies in the catalog that are UDGs, with effective radii exceeding 1.5 kpc and mean effective surface brightnesses fainter than 24 mag arcsec^{-2}.

2.5. Physical and Observed Properties of the Samples

As this work centers around the analysis of three similarly processed but heterogeneously selected samples, it is informative to compare the physical and observed properties of the three samples. As the derivation of many physical properties hinges on a measure of galaxy distance, we first address existing redshift measurements for the samples.

A forthcoming analysis of the HSC-SSP catalog estimates a median source distance of ~60 Mpc (J. Greco et al., 2021 in preparation); we adopt this value in this analysis. We show the soft boundaries of the absolute r-band magnitude and effective radius distributions over the LSBG sample if we assume a fixed distance of 60 Mpc in blue with Figure 3. We show the analogous metrics for the Coma cluster UDG sample of Alabi et al. (2020) by the orange dashed histogram. We stress that the sample range over these physical properties is provided only to contextualize the general nature of the sample, and should not be interpreted as estimates of the absolute magnitude or effective radius of the LSBGs. This approach will not, for example, populate the tails of the absolute magnitude and effective radius distribution. We note that even if all galaxies were assumed to be at a distance of 100 Mpc, the median absolute r-band magnitude would still be $\langle M_r \rangle = -14.8$ ($\langle M_r \rangle = -13.7$ at $d = 60$ Mpc).

We do not have a distance estimate for the Tanoglidis et al. (2021) sample; because the sample selection is modeled after that of Greco et al. (2018), we assume that the distribution over absolute magnitude and effective radius is similar. Due to the difference in the surface brightness limits of DES and HSC-SSP (see Figure 2), this assumption is likely incorrect in the details, but should hold as an order of magnitude estimate.

Finally, due to the initial H I selection of the ALFALFA/Legacy sample, H I redshifts have been measured for each galaxy; details of these measurements can be found in Leisman et al. (2017) and Janowiecki et al. (2019). The r-band absolute magnitude and effective radius distributions for the H I-selected sample are shown in Figure 3 by unfilled orange histograms. We find that the H I-selected sample tends to be more luminous
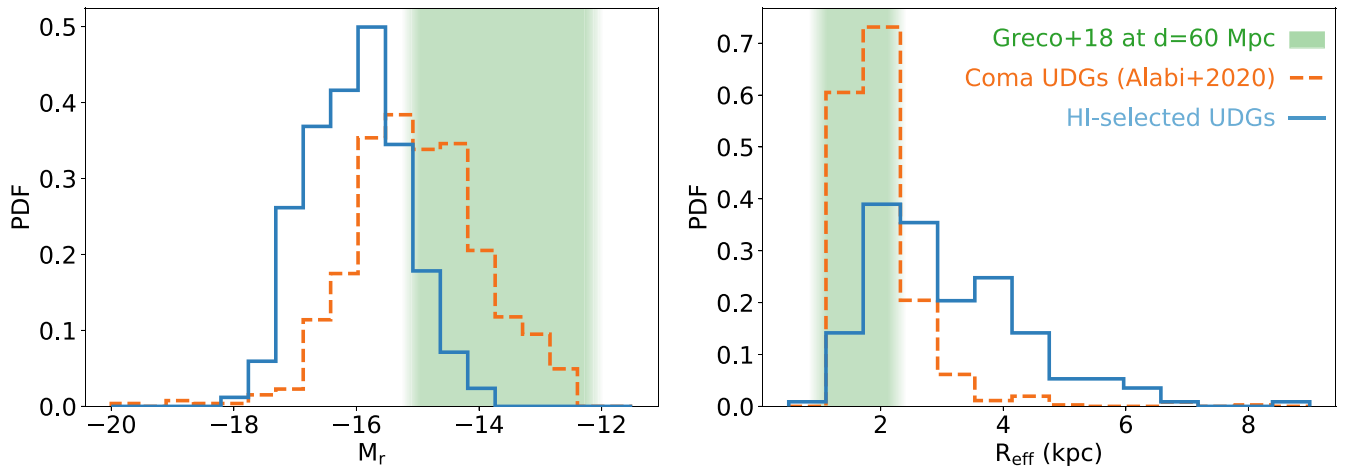
Figure 3. We compare the distribution in absolute *r*-band magnitude and physical effective radius for the samples examined in this work. We show in green a contextualization of the Greco et al. (2018) HSC-SSP LSBG sample M_r and effective radius distribution as computed by assuming that all galaxies in the LSBG sample are at the cross-correlation median distance of 60 Mpc (J. Greco et al., 2021 in preparation). We show the same quantities computed for the H I-selected sample using the H I redshifts measured by Leisman et al. (2017) and Janowiecki et al. (2019) by the unfilled blue histogram. Finally, we show the Coma Cluster UDGs of Alabi et al. (2020) by the unfilled orange histogram (dashed lines). Though the DES sample is not shown in this figure, we expect that the DES sample is similar in mass and size to the HSC sample.
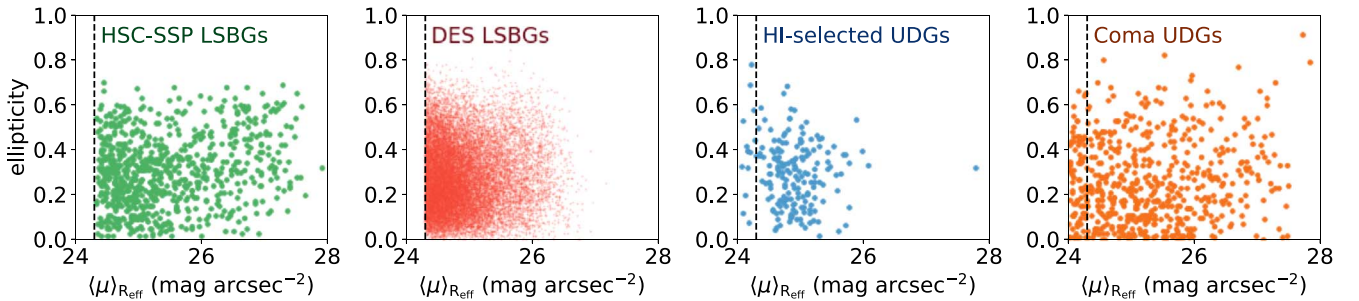
Figure 4. Ellipticity vs. surface brightness for the four samples considered in this work, as labeled. We use these diagnostic plots to demonstrate that the distribution of ellipticity does not change over the range of surface brightnesses considered in this work, supporting our assumption that the full sample can be characterized by a single distribution in three-dimensional shape, and to visually illustrate the different depths of the four samples.

and larger than both the HSC and Yagi et al. (2016) samples. This is likely because the H I selection was sensitive only to the most massive H I disks, as well as because the selection employed a more stringent physical size requirement than that of Greco et al. (2018) (when assuming the median source distance of $d = 60$ Mpc). We also note that the H I-selected sample is significantly more distant than the HSC sample, which is consistent with the H I-selected sample being more luminous.

In Figure 4, we show the distribution of mean effective surface brightness versus ellipticity for the four samples considered in this work. These panels show first that there is no global trend in ellipticity as a function of surface brightness, supporting the assumption that each sample can be characterized by a singular unified distribution over three-dimensional shape. Indeed, the covariance between the surface brightness and ellipticity within our surface brightness limits is minimal or consistent with zero for all four samples: $\mathrm{Cov}(\langle\mu\rangle_{R_{\mathrm{eff}}}, \epsilon)_{\mathrm{HSC}} = 2.80^{+3.06}_{-3.37} \times 10^{-3}$ mag arcsec^{-2}, $\mathrm{Cov}(\langle\mu\rangle_{R_{\mathrm{eff}}}, \epsilon)_{\mathrm{DES}} = -1.10^{+0.35}_{-0.34} \times 10^{-3}$ mag arcsec^{-2}, $\mathrm{Cov}(\langle\mu\rangle_{R_{\mathrm{eff}}}, \epsilon)_{\mathrm{HI}} = -2.74^{+3.65}_{-3.77} \times 10^{-3}$ mag arcsec^{-2}, and $\mathrm{Cov}(\langle\mu\rangle_{R_{\mathrm{eff}}}, \epsilon)_{\mathrm{Coma}} = 1.32^{+0.70}_{-0.69} \times 10^{-2}$ mag arcsec^{-2}.

We note that the *r*-band photometry of the HSC sample is from the HSC *r* band, the photometry of the Yagi et al. (2016) sample is from the Suprime *R* band, and the photometry of the

H I sample is from the Legacy Survey *r* band. To gauge the effect of the differences between these bands, we compute synthetic photometry through each bandpass for a set of model dwarf spectra taken from dwarfs in the catalog of Muzzin et al. (2013). We find that the difference between the bands is minimal, with an average difference between the HSC and Suprime *r* bands of $(\langle\Delta m\rangle, \sigma_{\Delta m}) = 0.00 \pm 0.03$ and an average difference between the HSC and DECam *r* bands of $(\langle\Delta m\rangle, \sigma_{\Delta m}) = -0.01 \pm 0.04$.

3. Intrinsic Shape Inference

The distribution of intrinsic shapes may be inferred from the observed ellipticity distribution of a galaxy population by assuming that the galaxies can, at fixed radius, be described by ellipsoids with semi-principal axis diameters *A*, *B*, and *C*, where $C \leqslant B \leqslant A$. In Figure 5, we show the positions in B/A–C/A space and 3D renderings of three archetypal examples: a disk (blue), prolate (green), and spheroid (red). We also assume that the LSBG samples can be described by a single multivariate normal distribution over the principal axis ratios B/A and C/A. This method is detailed in Kado-Fong et al. (2020b); we summarize the salient points below.

The projected axis ratio, $q = b/a$ where *b* and *a* are, respectively, the semiminor and semimajor axes of the projected ellipse, for a given ellipsoid is determined solely by the observer's
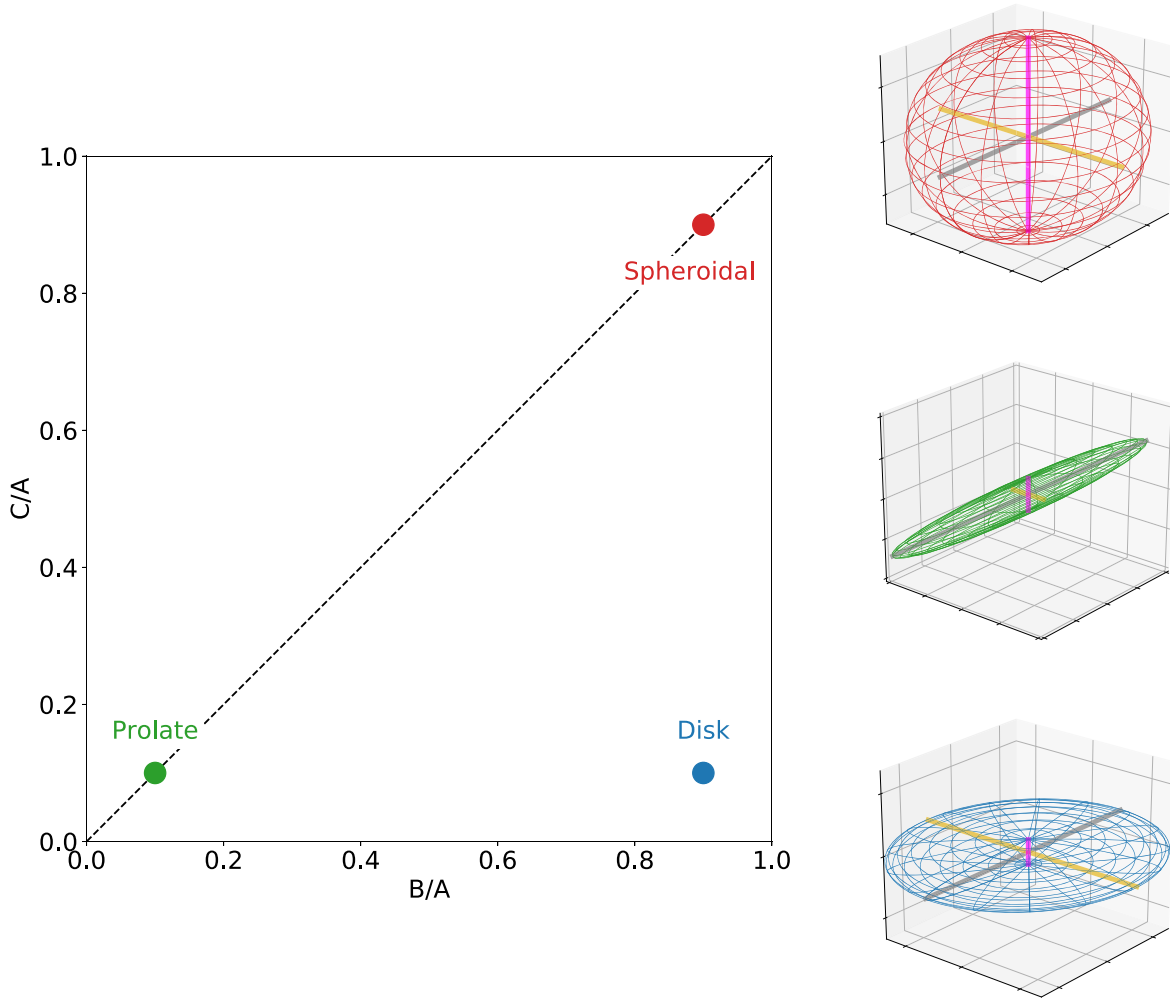
Figure 5. A schematic diagram to illustrate movement in the B/A vs. C/A plane. The red, green, and blue points show the position of an archetypal spheroidal, prolate, and disky ellipsoid, respectively. The axis ratios are $(B/A,C/A) = (0.9,0.9)$, $(0.1,0.1)$, and $(0.9, 0.1)$ for the three cases. At right, we show a three-dimensional representation of the ellipsoid that corresponds to each case in the corresponding color. We additionally show the principal axes A, B, and C as gray, gold, and magenta lines in each panel.

viewing angle, (θ, ϕ), i.e., $q = \mathcal{F}(B/A, C/A, \theta, \phi)$. The analytic expression for $\mathcal{F}$ was presented by Simonneau et al. (1998), and is reproduced below. First, $(ab)^2$ and $(a^2 + b^2)$ can be rewritten as follows:

$$a^2 b^2 = f^2 = (C \sin\theta \cos\phi)^2 + (BC \sin\theta \sin\phi)^2 + (B \cos\theta)^2, \tag{2}$$

$$a^2 + b^2 = g = \cos^2\phi + \cos^2\theta \sin^2\phi + B^2(\sin^2\phi + \cos^2\theta \cos^2\phi) + (C \sin\theta)^2. \tag{3}$$

We now define the quantity h to be

$$h \equiv \sqrt{\frac{g - 2f}{g + 2f}}, \tag{4}$$

such that it may be shown that

$$\frac{b}{a} = \frac{1 - h}{1 + h}. \tag{5}$$

Because the distribution of viewing angles is known to be isotropic on the surface of the sphere, we can predict the projected distribution of q given a choice of intrinsic shape

distribution characterized by $\vec{\alpha}$ by sampling ϕ and θ as follows:

$$\phi \sim \mathcal{U}[0, 2\pi]$$
$$\nu \sim \mathcal{U}[0, 1]$$
$$\theta = \cos^{-1}(2\nu - 1). \tag{6}$$

However, we must also consider the bias imposed by surface brightness selection inherent in the selection method of LSBG samples. To create a LSBG sample, one must necessarily make a cut in surface brightness. Because galaxies are three-dimensional objects, it is possible that some galaxies will be considered LSB only at certain viewing angles. This effect is maximized for disky ($C < B \sim A$) galaxies, wherein the observed surface brightness will be systematically lower for face-on views than for edge-on views. An attempt to invert the 3D shape of such a sample without accounting for this potential incompleteness could then result in severely biased results.

If one assumes that the LSBGs are well described by a Sérsic profile with $n = 1$, the observed surface brightness of an object as a function of viewing angle is exactly prescribed by the intrinsic shape of the object and its intrinsic stellar density. We find that this assumption is well supported by the data (see Figure 6), and adopt a fixed profile with $n = 1$ for this work. We neglect the effect of dust on the observed shape in this
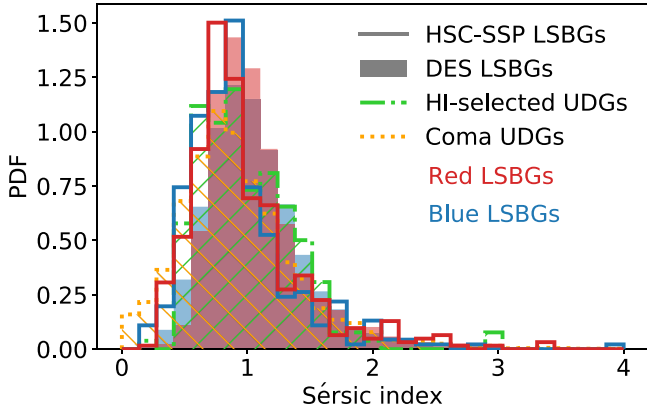
Figure 6. The distribution of Sérsic indices for the red ($g - i > 0.64$) and blue ($g - i < 0.64$) HSC LSBGs (Greco et al. 2018, filled histograms) and DES LSBGs (Tanoglidis et al. 2021, unfilled histograms). Though there is a an offset between the HSC and DES measurements, there is no significant difference between the red and blue subsets of each sample. We also show the H I-selected (dotted–dashed green) and Coma (dotted orange) UDGs, which are also consistent with the LSBG distribution of Sérsic indices.

framework—due to the low masses, large effective radii, and low surface densities of the objects in question, it is unlikely that dust will significantly impact the observed shape at $1R_{\rm eff}$. With these assumptions in hand, by including additional parameters to describe the distribution of intrinsic density of the LSBGs, we can take into account this potential surface brightness incompleteness when inferring the intrinsic 3D shapes of the LSBG samples.

To do so, we compute the projected surface brightness within $R_{\rm eff}$ for a given choice of shape (B/A, C/A), viewing angle (θ, ϕ), and intrinsic density ρ_0. We find that using three-dimensional $R_{\rm eff,3D}$ (as opposed to the projected $R_{\rm eff}$) does not strongly affect our results, and considerably reduces computation time, so choose to use the three-dimensional $R_{\rm eff,3D}$ in this calculation. We first compute the three-dimensional density using the analytic approximation for the three-dimensional Sérsic density profile of Prugniel & Simien (1997):

$$\rho\left(\frac{r}{R_{\rm eff,3D}}\right) = \rho_0\left(\frac{r}{R_{\rm eff,3D}}\right)^{-p_n} \exp\left[-b_n\left(\frac{r}{R_{\rm eff,3D}}\right)^{1/n}\right], \quad (7)$$

where

$$p_n = 1 - \frac{0.549}{n} + \frac{0.055}{n^2} \quad (8)$$

and $\Gamma(2n) = 2\gamma(2n, b_n)$. We rotate this grid to align with the line of sight defined by (θ, ϕ) using the rotation matrix

$$\mathbb{A} = \begin{bmatrix} \cos\phi & \cos\theta\sin\phi & \sin\theta\sin\phi \\ -\sin\phi & \cos\theta\cos\phi & \sin\theta\cos\phi \\ 0 & -\sin\theta & \cos\theta \end{bmatrix}$$

such that the rotated coordinates $\mathbf{r}_r = \mathbb{A}\mathbf{r}$ align with the line of sight along the z axis. We then measure the mean surface brightness within $1R_{\rm eff,3D}$. To reduce computation time, we pre-compute the surface brightness as a function of shape (B/A, C/A) and viewing angle (θ, ϕ), sampling uniformly over parameter space in a grid of size 30^4. We then linearly interpolate over this grid during inference; we find that our results are not significantly affected by the adoption of this approximation scheme.

In order to jointly fit the ellipticity and mean surface brightness distribution of our galaxy samples, we modify the Poisson likelihood used in Kado-Fong et al. (2020b) to include the surface brightness distribution:

$$\ln p(\mathbf{q}_{\rm obs}, \langle\vec{\mu}\rangle_{R_{\rm eff,obs}}|\vec{\alpha}) = \sum_i n_i \ln m_i - m_i - \ln n_i!$$

$$\vec{\alpha} = (Q_0, S_0, \mu_{\rho_0}, \sigma_{Q_0}, \sigma_{S_0}, \sigma_{\rho_0}), \quad (9)$$

where $Q = B/A$ and $S = C/A$. In our notation, Q_0 and σ_{Q_0} (S_0 and σ_{S_0}) correspond to the mean and standard deviation of the axis ratio B/A (C/A) assuming a bivariate Gaussian as the functional form for the underlying intrinsic shape distribution. We find that the ellipticity distributions of our LSBG samples (as well as the HSB dwarf samples of Kado-Fong et al. 2020b) are able to be well reproduced by the relatively simple bivariate Gaussian model. We thus do not consider more complex functional forms in this work, though we have explored a model that includes size-shape covariance in Kado-Fong et al. (2020b) and the effect of a bimodal ground truth distribution on our bivariate and unimodal Gaussian modeling in an upcoming work (Kado-Fong et al., submitted). The observed count in bins of axis ratio is given as n_i, and m_i is the predicted count in the same range. We do not consider draws that lie outside of the observable boundaries ($\epsilon > 0.7$ for the HSC and DES samples or below the surface brightness limit)—that is, the imposed absence of HSB or low q sources does not impact the likelihood computation. We adopt axis ratio bins of $dq = 0.05$ and mean surface brightness bins of $d\langle\mu\rangle_{R_{\rm eff}} = 0.5$ for all inferences in this work.[14]

We use the Markov Chain Monte Carlo ensemble sampler implemented in emcee (Foreman-Mackey et al. 2013) to sample efficiently from the posterior $\ln p(\vec{\alpha}, \mathbf{q}_{\rm obs}, \langle\vec{\mu}\rangle_{R_{\rm eff,obs}})$. We implement a flat prior over the physical range of all our fitted parameters; that is,

$$p(Q_0) = \begin{cases} 1 & \text{if } 0 < Q_0 < 1 \\ 0 & \text{otherwise.} \end{cases} \quad (10)$$

We additionally constrain $S_0 \leqslant Q_0$ to maintain the order of axes,

$$p(S_0) = \begin{cases} 1 & \text{if } (0 < S_0 < 1) \wedge (S_0 \leqslant Q_0) \\ 0 & \text{otherwise.} \end{cases} \quad (11)$$

When sampling from a given α, we disregard ellipsoids where $C > B$. We only require that the mean surface brightness is a positive value, i.e.,

$$p(\rho_0) = \begin{cases} 1 & \text{if } \mu_{\rho_0} > 0 \\ 0 & \text{otherwise.} \end{cases} \quad (12)$$

Similarly, we require the standard deviations of B/A and C/A are a positive value less than $\sigma = 0.5$:

$$p(\sigma_X) = \begin{cases} 1 & \text{if } 0 < \sigma_X < 0.5 \\ 0 & \text{otherwise} \end{cases} \quad (13)$$

---

[14] We previously found in Kado-Fong et al. (2020b) that the choice of bin size does not strongly affect inference results.

for $X \in \{B, C\}$. We only require σ_{ρ_0} to be positive:

$$p(\sigma_{\rho_0}) = \begin{cases} 1 & \text{if} \quad 0 < \sigma_{\rho_0} \\ 0 & \text{otherwise.} \end{cases} \quad (14)$$

We run all inferences for at least 500 steps over 32 walkers, and discard the first 250 steps of each walker. We manually confirm that the chains have converged. We also extend the mock recovery tests of Kado-Fong et al. (2020b) to include this joint inference scheme—we present the results of these tests in the Appendix. We find that the joint inference reduces the inference precision for the spheroid and prolate populations, where the surface brightness changes little with viewing angle, but increases the inference precision for the disk population, where the surface brightness changes strongly with viewing angle.

4. Results

We show the results of the intrinsic shape inference in Figure 7. From top left, we show the inference for the HSC-SSP LSBG sample of Greco et al. (2018), the full DES sample of Tanoglidis et al. (2021), the H I-selected sample originally constructed by Leisman et al. (2017) and Janowiecki et al. (2019), the blue $(g - i < 0.64)$ DES LSBGs, and the red $(g - i \geqslant 0.64)$ DES LSBGs. For the DES sample and subsamples, we show the inference results when surface brightness and ellipticity are jointly fit (unfilled turquoise contours) and when only ellipticity is considered (filled orange histogram). We find that the joint fit does not converge for the HSC-SSP and H I-selected samples due to the relatively small sample sizes (a result that is expected based on the tests that we ran with mock galaxy populations, see the Appendix and Kado-Fong et al. 2020b); we thus only show the results of the ellipticity-only inference. In all cases, the joint maximum a posteriori (MAP) estimate and ellipticity-only MAP estimates are within very good agreement, indicating that the observed surface brightness cut does not significantly bias the observed ellipticity distribution. To rephrase this point, we find that because the intrinsic shapes of the LSBGs are relatively round, the observed surface brightness does not correlate strongly with the ellipticity. We additionally show the distribution of model surface brightnesses and ellipticities (along with their observational counterparts) for the DES samples in Figure 8. We find that the surface brightness distribution of the red LSBGs is not as well fit in our inference—this likely indicates that the underlying surface brightness distribution is not well described by a Gaussian. However, through tests with a uniform surface brightness distribution we find that our results are robust against a change in the assumed parametric form of the underlying surface brightness distribution. Furthermore, disky shapes are required to produce a strong correlation between surface brightness and ellipticity, and it is highly unlikely based on previous studies of dwarfs (Sánchez-Janssen et al. 2010; Burkert 2017; Rong et al. 2020; Kado-Fong et al. 2020b; Carlsten et al. 2021) and higher mass galaxies (see, e.g., Padilla & Strauss 2008) that the red LSBGs would be diskier than the blue LSBGs. We present the MAP estimates, along with associated uncertainties, for all inference results in Table 1.

Though the numbers of the HSC-SSP and H I-selected samples preclude a division as a function of galaxy color, we can use these samples to confirm that our method returns consistent results for both samples. For the HSC sample, this is a simple confidence check with a deeper sample—assuming that the shapes measured in DES are not significantly impacted by the depth of the imaging, the samples should return a consistent result, as they are selected using similar methods. The concordance of the H I-selected UDG intrinsic shape distribution is somewhat more intriguing, as the sample is more luminous and selected to have significant stores of cold gas and is likely a more luminous sample (see Figure 3)—we defer a more complete discussion of this result to Section 5.1.

4.1. Intrinsic Shape versus Color and Environment

The correlated bimodality of morphology and color is a well-established facet of the galaxy population for massive galaxies (see, e.g., Padilla & Strauss 2008) At dwarf masses, there is evidence that the bimodality persists in massive dwarfs (Kado-Fong et al. 2020b), with some evidence that the structural properties may begin to converge at lower masses (Carlsten et al. 2021). Blue galaxies are typically also disk galaxies, while red galaxies are ellipticals. It is thus of interest to ask whether the same bimodality is observed in the DES LSBG sample (the HSC-SSP sample is not large enough to split into two samples).

As shown in Figure 7, we find no evidence for a significant difference in intrinsic shape distribution of the red and blue LSBGs of the DES sample. This result is not unexpected; as shown in Figure 6, the Sérsic index distribution of red and blue LSBGs are also remarkably similar for both the DES and HSC-SSP samples, as well as the H I-selected sample. This is in strong contrast to more massive galaxies, wherein the Sérsic index distributions are markedly different between the red and blue galaxy populations.

We also find that the three-dimensional shapes of the UDGs are largely unchanged as a function of environment, as shown by contrasting the Coma UDGs (rightmost panel, second row in Figure 9) to the blue LSBGs and H I-selected galaxies, both of which are unlikely to be dominated by dwarfs in cluster environments. Indeed, this result is in agreement with previous measurements of cluster UDG shapes, as will be further discussed in Section 5.1.

5. Discussion

Although the existence of LSBGs has been known observationally for some time, the path through which this tail of the galaxy population is formed remains unclear. UDGs in the field have been proposed to form via a variety of processes, including that they may populate high-spin halos (Dalcanton et al. 1997; Amorisco & Loeb 2016; Liao et al. 2019), that they are formed via star formation feedback (Jiang et al. 2019; Chan et al. 2018), or that they are the end products of early mergers that cause star formation to migrate to large radii (Wright et al. 2021). High-density environments provide potential alternate pathways to UDG formation via environmental effects such as ram pressure stripping and tidal heating (Jiang et al. 2019; Tremmel et al. 2020). Here, we consider the implications of the inferred intrinsic shapes of our LSBG samples both in conjunction with previous observational works and in comparison to contemporary theoretical predictions.

5.1. Comparison to Observations

We first compare our inferred LSBG shape distribution to results from the literature. We probe both the potential influence of environment by comparing to the inferences of cluster and group UDG shapes from Burkert (2017) and Rong et al. (2020)
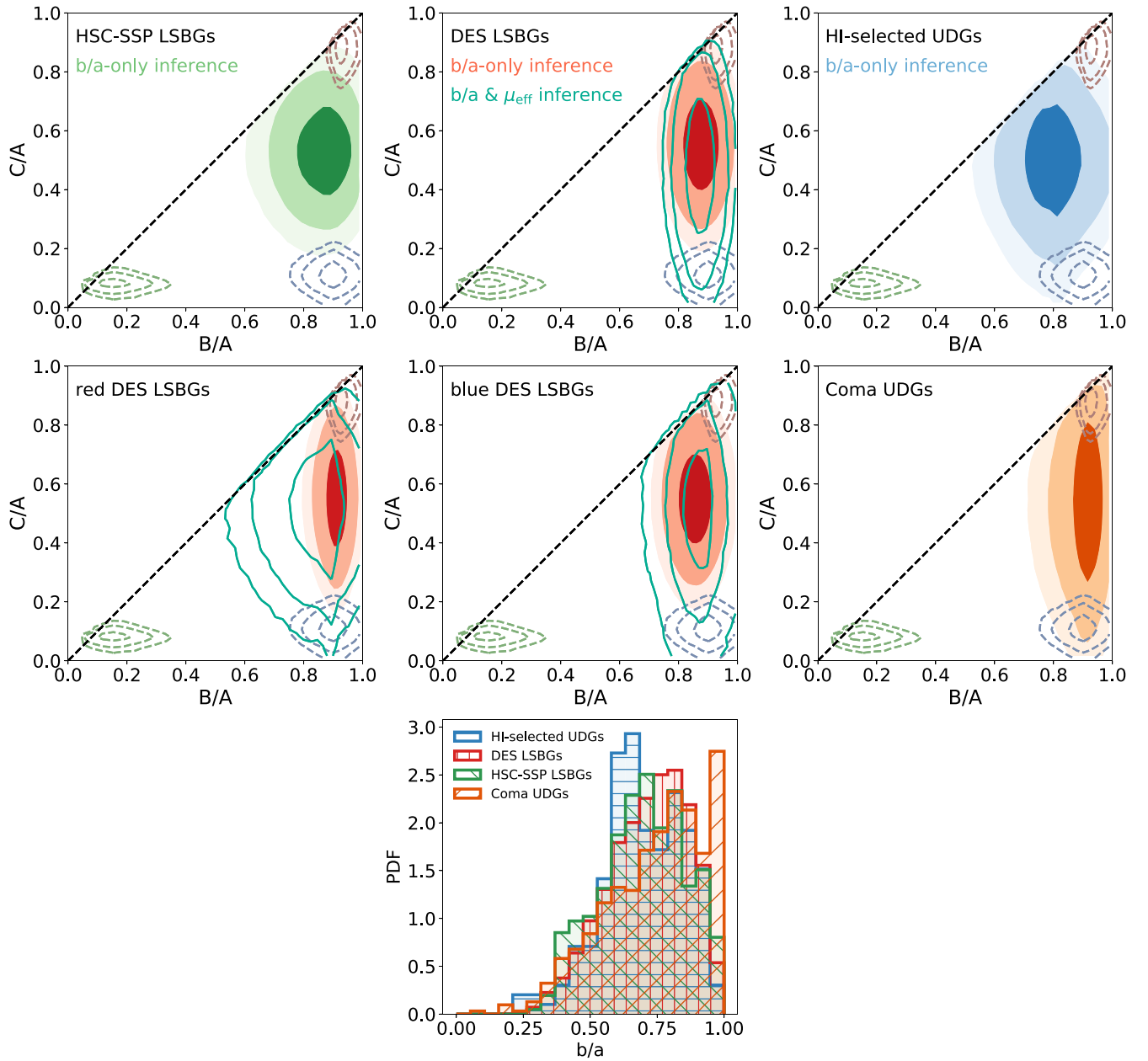
Figure 7. The inferred intrinsic axis ratios for the galaxy samples considered in this work: from the top left, the HSC-SSP sample of Greco et al. (2018) (green), the DES sample of Tanoglidis et al. (2021) (red), the H I-selected galaxies of Janowiecki et al. (2019) (blue), the red galaxies of the DES sample ($g − i < 0.64$), the blue galaxies of the DES sample ($g − i \geqslant 0.64$), and the Coma UDGs of Alabi et al. (2020) (orange). The filled contours show the inference results when only ellipticity is fit, while the unfilled turquoise contours in the DES panels show the inference results when both surface brightness and ellipticity are fit. Both sets of contours enclose 0.34^2, 0.68^2, 0.95^2, and 0.99^2 of the population (corresponding to 0.5σ, 1σ, 2σ, and 3σ of a multivariate normal). In the panels showing the inferred intrinsic axis distributions, the unfilled dashed contours show the results of recovery tests for a disky (blue), prolate (green), and spheroidal (red) population via ellipticity-only inference as presented in Kado-Fong et al. (2020b). The dashed black line shows the definitional $B = A$ boundary. The bottom right panel shows the projected axis ratio ($b/a = 1-\epsilon$) for the three samples used in this work. For visual clarity, we do not show the projected axis ratio distributions for the blue and red subsets of the DES sample here, but both are shown in Figure 8. Crucially, there is no significant difference between the inferred shapes of the joint models and ellipticity-only models, indicating that incompleteness due to surface brightness limits does not induce a significant bias in the observed ellipticity distributions of the LSBGs.

and the potential influence of surface density by comparing to the normal dwarf (meaning higher surface brightness) spectroscopic sample of Kado-Fong et al. (2020b), as shown in Figure 9.

We find remarkably good agreement between our results and those of Rong et al. (2020), who infer the shape distribution of UDGs in high-density group and cluster environments. We also see good agreement with the results of Burkert (2017), when it is considered that this work did not allow for triaxiality (i.e., enforced $B/A = C/A$). Though the environments of the DES

and HSC-SSP samples are not known on the level of individual systems, the spatial distribution of the red and blue LSBGs of both samples suggest that the red LSBGs are more clustered than the blue LSBGs, which have a nearly homogeneous distribution on the sky (Greco et al. 2018; Tanoglidis et al. 2021). This indicates that red LSBGs are relatively more likely to live in high-density environments, while blue LSBGs are relatively more likely to live in the field. We can thus say that, on average, the blue LSBGs live in lower density environments
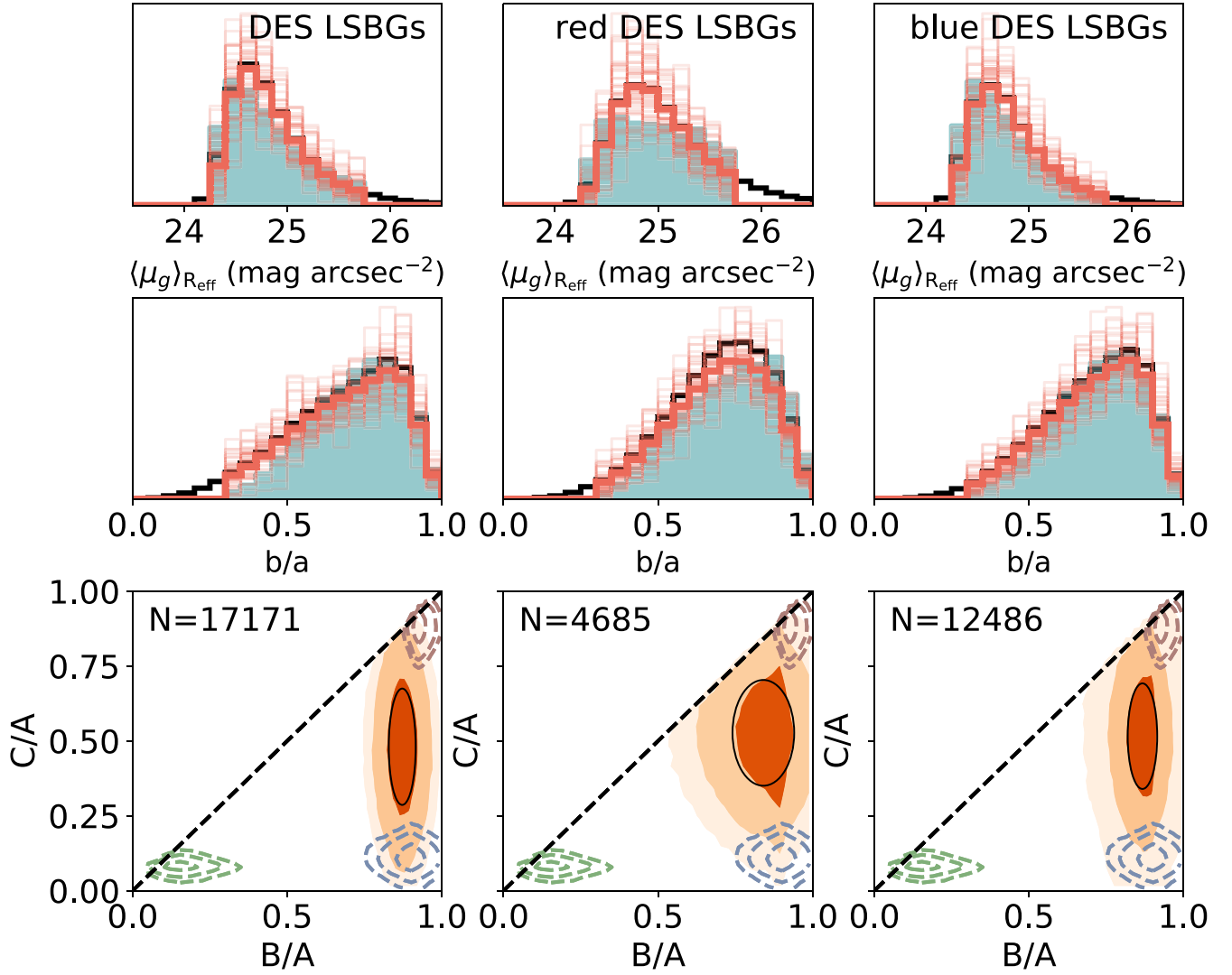
Figure 8. Recovery results for joint inference of the samples; from left to right: the full DES sample, red DES LSBGs, and blue DES LSBGs. *Top row*: The surface brightness distribution for each population. The thick orange curve shows our posterior sample (thin orange curves show individual pulls from the posterior). The solid teal histograms show the observed population. Unfilled black histograms show model projections that fall outside of the sample surface brightness limits. *Middle row*: the same for the ellipticity distributions. *Bottom row*: we show the intrinsic axis ratio distribution of the posterior sample as filled orange contours. The MAP results are shown by black ellipses. We note that the joint inference does not converge for the HSC-SSP and H I-selected samples due to the low number of objects; we thus use only the ellipticity-only inference for these samples.

Table 1
Median Values and 95% Credible Intervals of Inferred Intrinsic Shape Parameters

Associated Figure	Sample	Q_0 (B/A)	σ_{Q_0}	S_0 (C/A)	σ_{S_0}	T_0	ρ_0	σ_{ρ_0}
Figure 7	HSC-SSP LSBGs	$0.85^{+0.09}_{-0.07}$	$0.07^{+0.07}_{-0.07}$	$0.53^{+0.04}_{-0.04}$	$0.13^{+0.04}_{-0.03}$	$0.38^{+0.18}_{-0.24}$	⋯	⋯
	DES LSBGs	$0.88^{+0.01}_{-0.02}$	$0.05^{+0.02}_{-0.01}$	$0.55^{+0.01}_{-0.01}$	$0.14^{+0.01}_{-0.01}$	$0.34^{+0.07}_{-0.05}$	⋯	⋯
	H I-selected UDGs	$0.80^{+0.10}_{-0.06}$	$0.09^{+0.05}_{-0.08}$	$0.50^{+0.08}_{-0.06}$	$0.16^{+0.14}_{-0.06}$	$0.50^{+0.14}_{-0.24}$	⋯	⋯
	Red DES LSBGs	$0.91^{+0.03}_{-0.03}$	$0.03^{+0.02}_{-0.03}$	$0.55^{+0.02}_{-0.02}$	$0.14^{+0.01}_{-0.02}$	$0.25^{+0.08}_{-0.08}$	⋯	⋯
	Blue DES LSBGs	$0.85^{+0.02}_{-0.03}$	$0.05^{+0.02}_{-0.02}$	$0.55^{+0.01}_{-0.01}$	$0.14^{+0.01}_{-0.01}$	$0.39^{+0.07}_{-0.06}$	⋯	⋯
	Coma UDGs	$0.90^{+0.07}_{-0.07}$	$0.04^{+0.06}_{-0.04}$	$0.54^{+0.06}_{-0.06}$	$0.23^{+0.05}_{-0.05}$	$0.26^{+0.18}_{-0.18}$	⋯	⋯
Figure 8	DES LSBGs	$0.87^{+0.02}_{-0.49}$	$0.05^{+0.03}_{-0.04}$	$0.48^{+0.04}_{-0.03}$	$0.19^{+0.02}_{-0.12}$	$0.31^{+0.10}_{-0.08}$	$0.67^{+0.11}_{-0.50}$	$0.40^{+0.05}_{-0.21}$
	Red DES LSBGs	$0.83^{+0.06}_{-0.42}$	$0.11^{+0.11}_{-0.10}$	$0.53^{+0.45}_{-0.08}$	$0.17^{+0.05}_{-0.06}$	$0.43^{+0.26}_{-0.19}$	$0.20^{+0.10}_{-0.08}$	$0.50^{+0.08}_{-0.28}$
	Blue DES LSBGs	$0.86^{+0.03}_{-0.05}$	$0.05^{+0.03}_{-0.03}$	$0.52^{+0.04}_{-0.04}$	$0.18^{+0.03}_{-0.05}$	$0.35^{+0.10}_{-0.09}$	$0.60^{+0.16}_{-0.21}$	$0.47^{+0.13}_{-0.08}$

Note. The top section shows the results of the ellipticity-only inference, while the bottom section shows the results of the surface brightness and ellipticity joint fit. In all cases, the first 250 steps of each walker are discarded. For ease of comparison with literature results, we also report T_0, the median triaxial ($T = (1 - (B/A)^2)/(1 - (C/A)^2)$), as calculated by sampling the inferred shape distributions.
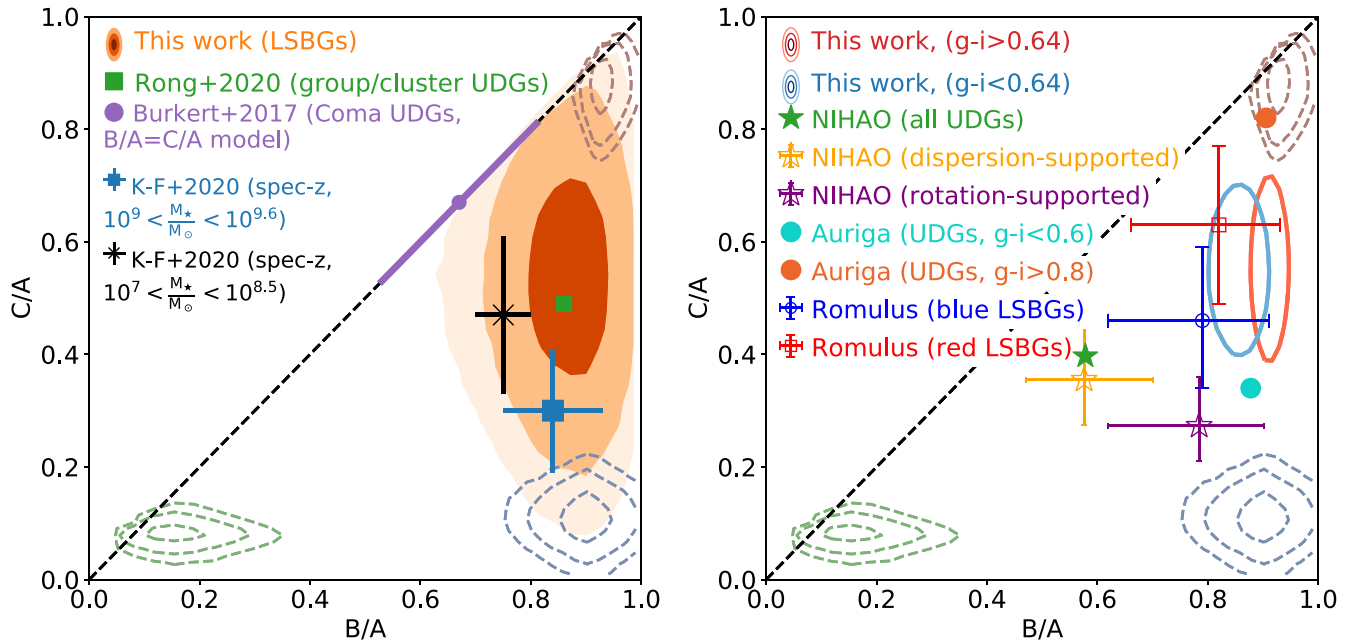
Figure 9. *Left*: A comparison between the results presented in this work (filled orange contours) and observational results from the literature. Our results are in good agreement with the group/cluster UDG samples of Burkert (2017) (who assumes a non-triaxial model where $B/A = C/A$) and Rong et al. (2020), indicating that the intrinsic shape distribution of LSBGs is not strongly affected by their environment. We also compare our results to those of the normal HSB dwarf populations at $1R_{\rm eff}$ presented in Kado-Fong et al. (2020b). We find that the LSBG sample is significantly rounder (higher C/A) than the massive dwarfs of Kado-Fong et al. (2020b). Error bars on the HSB points show the inferred 1σ dispersion of the HSB sample, not the error on the mean values. *Right:* A comparison between the inferred intrinsic shapes of red and blue LSBGs (unfilled red and blue contours, respectively) presented in this work and theoretical predictions from the literature. For visual clarity, we show only the contours that contain 68% of our inferred LSBG shapes in order to be consistent to the plotted error bars of the Romulus and NIHAO simulations, for which the error bars span the 16th–84th percentiles. We find that the intrinsic shape distributions vary significantly between the simulations considered. In particular, Auriga (Liao et al. 2019) predicts a strong shape divergence between blue and red UDGs, while NIHAO (Jiang et al. 2019; Cardona-Barrero et al. 2020) predicts significantly more triaxial (for dispersion-dominated UDGs) or flatter (for rotation-supported UDGs) shapes than those inferred from observed LSBGs. Romulus appears to well produce the shape distribution of blue LSBGs, but overpredicts the shape evolution between blue and red LSBGs.

than the samples of Burkert (2017) and Rong et al. (2020). Because these literature samples are focused on large groups and clusters, it is also likely the case that the typical red LSBG lives in a lower density environment than Burkert (2017) and Rong et al. (2020), but in a higher density environment than the typical blue LSBG. The concordance of shapes between all these samples then indicates that the local environment does not play a key role in determining the intrinsic shape of LSBGs.

Next, we compare the results of the LSBG galaxy sample to those of the spectroscopic normal dwarf sample of Kado-Fong et al. (2020b). These dwarfs are drawn from SDSS and Galaxy and Mass Assembly (GAMA) spectroscopic surveys. GAMA, the deeper of these surveys, has an effective surface brightness limit of $\mu_{\rm r,eff} \sim 24$ mag arcsec^{-2} (Baldry et al. 2012), meaning that the spectroscopic dwarf sample is nearly disjoint in surface brightness with the LSBG samples. Kado-Fong et al. (2020b) finds evidence that the intrinsic shape of dwarf galaxies changes as a function of mass—in particular, that dwarfs at $M_\star \lesssim 10^{8.5}$ are relatively more spheroidal than their higher mass analogs. To make a rough estimate of the stellar masses of our LSBG samples, we adopt a singular distance of 60 Mpc for the HSC-SSP sample (as informed by the cross-correlation analysis in J. Greco et al., 2021 in preparation), and estimate the mass-to-light ratio $(M/L)_i$ from the $(g-i)$ colors presented in Greco et al. (2018) and the color relations of Bell et al. (2003). We find that, for this rough approximation, the mean stellar mass of the HSC-SSP sample is roughly $\log(M_\star/M_\odot) \sim 7.5$. Our HSC and DES LSBG samples are thus most similar in stellar mass to the lowest mass bin of $7.5 < \log_{10}(M_\star/M_\odot) < 8.5$ in Kado-Fong et al. (2020b). Indeed,

we find that these low mass, HSB dwarfs are relatively oblate and spheroidal, similar to the LSBG samples However, despite being likely more luminous than the HSC and DES samples (see Figure 3), the H I-selected sample is also characterized by oblate spheroidal shapes. This is in contrast to the observed mass evolution of normal dwarfs, wherein the higher mass dwarfs maintain well-formed, albeit thick, disks. We thus suggest that the LSBGs may be thicker (in C/A) than the equivalent HSB galaxy sample—this effect is most distinct when considering that the more luminous H I-selected sample is also characterized by oblate spheroidal shapes. However, the incompleteness of the HSB sample at low ($M_\star \lesssim 10^8 M_\odot$) masses and the uncertainties in the stellar mass distribution of the HSC and DES samples suggest that more complete samples of HSB dwarfs, along with more distance determinations for LSBG dwarfs, are needed to secure this result.

Taken all together, the results presented in this work in conjunction with literature results from group/cluster UDGs and normal dwarfs shed new light on the structure formation of LSBGs. First, the concordance of shapes between LSBGs as a function of environment implies that the formation mechanism of cluster and field LSBGs does not produce drastically different intrinsic shapes. Second, we suggest that LSBGs and UDGs may be rounder than their HSB counterparts, and possibly unable to support well-formed stellar disks where HSB dwarfs succeed in maintaining them.

5.2. Comparison to Simulations

Having contextualized our results with previous observational results from the literature, we now compare our findings to

predictions from the UDG populations produced in cosmological simulations. There are several paths to UDG formation proposed by various simulations; we focus here on the Auriga simulation (Liao et al. 2019), the NIHAO simulation (Jiang et al. 2019), and the Romulus simulations (Tremmel et al. 2020; Wright et al. 2021).

The UDG formation path of the simulations differ significantly, and those differences manifest in the predicted intrinsic shape distribution of each simulation. The Auriga field UDGs form in high-spin halos (see also Dalcanton et al. 1997; Amorisco & Loeb 2016 who also form UDGs in the high-spin tail the halo population), while satellite UDGs form via a mixture of tidal effects and field UDG capture by massive halos. This results in a pronounced difference in the intrinsic shape distributions of the red and blue UDGs, wherein the blue Auriga UDGs are thick disks (turquoise point, right panel of Figure 9) and the red Auriga UDGs are spheroidal (orange point). This shape contrast is in disagreement with our results, which do not point to a significant bimodality in shape as a function of color or a significant population of disky UDGs at any mass. Furthermore, our results indicate that the H I-selected LSBG sample is puffier (higher C/A) than the HSB sample of Kado-Fong et al. (2020b) at similar stellar masses—this finding is also at odds with the theory that LSBGs form in the high angular momentum tail of the halo distribution function.

The Numerical Investigation of a Hundred Astrophysical Objects (NIHAO) simulations, meanwhile, predict that UDGs are formed in the field via supernovae feedback. These UDGs are characterized by particularly bursty star formation histories relative to the more compact galaxies in NIHAO (Di Cintio et al. 2017). Satellite UDGs are formed from infalling field UDGs and created from tidal effects. Though Jiang et al. (2019) do not compute the intrinsic shape distributions of satellite and field (or red and blue) UDGs separately, they do report the overall mean intrinsic principal axis ratios. We find that the NIHAO results are significantly more triaxial than our observed results. This excessive triaxiality is also seen in a subset of the galaxies in the Feedback In Realistic Environments (FIRE) simulation suite, which are also characterized by particularly bursty star formation histories (Chan et al. 2018, Kado-Fong et al., in preparation). Cardona-Barrero et al. (2020) further analyze the shape distribution of the NIHAO UDGs as a function of their stellar kinematics. They find in particular that the rotationally supported UDGs are characterized by more oblate ($B/A_{\rm rotation} > B/A_{\rm dispersion}$) and flatter disks. We find that these rotationally supported UDGs are, on average, flatter than our observed LSBG and UDG samples, similar to those found in the Auriga simulations.

The formation mechanisms for UDGs in the Romulus simulations stand in contrast to those presented in NIHAO and Auriga. Since Romulus cannot resolve high-density star formation and thus large outflows in dwarfs, feedback cannot drive their formation. However, upcoming comparison work between the Romulus simulations and the Marvel-ous Dwarfs, a zoom suite that succeeds in forming cored dwarf profiles via feedback with a force resolution of 60 pc and a dark matter (DM) (stellar) mass resolution of 6650 $M_\odot$ [420 $M_\odot$] (Munshi et al. 2021), does indicate that the UDG shapes of Romulus and Marvel-ous are broadly consistent (Van Nest et al. 2021). Thus, we do not expect that the intrinsic shapes of the LSBGs in Romulus are simply an effect of resolution. The Romulus

simulations furthermore do not find halo spin as a primary mechanism for UDG formation, as is the case in Auriga.

Both Wright et al. (2021) and Tremmel et al. (2020) explore alternative formation mechanisms in isolation and in a cluster environment. In particular, Tremmel et al. (2020) suggest that cluster UDGs are formed primarily through the dual effects of passive fading following quenching via ram pressure after early cluster infall and size evolution in the cluster environment. In the field, Wright et al. (2021) find that Romulus UDGs are formed via early major mergers that redistribute star formation to larger radii. Van Nest et al. (2021) will explore the shape evolution of UDGs in comparison to dwarfs in Romulus. We select LSBGs from Romulus25 (Tremmel et al. 2017) and RomulusC (Tremmel et al. 2019) on their central surface brightness and effective radius in a method similar to that in Tremmel et al. (2020), Wright et al. (2021). To best match the properties of the LSBG sample in this work, we impose a size cut of $R_{\rm eff} > 1$ kpc and a surface brightness cut of $\langle \mu \rangle_{R_{\rm eff}} > 24.3$ mag arcsec^{-2}. They are divided into blue and red populations based on their $g - i$ color using the same dividing value of $(g - i) = 0.64$ as the observational sample. The values shown in Figure 9 correspond to the median of each population with the error bars representing the 16th–84th percentile ranges. Although the Romulus LSBGs show slightly more intrinsic shape evolution as a function of their $(g - i)$ color, both the red and blue simulated LSBG populations are in reasonable agreement with our observed samples. We expect that the color-shape evolution seen in Romulus is partially driven by resolution effects: dwarfs are overquenched in the cluster environment of RomulusC (Tremmel et al. 2017), leading to overly red colors and an over-representation of cluster LSBGs at the red end of the color distribution. We thus conclude that the Romulus LSBGs are in the best agreement with the inferred observational shapes out of the simulation results considered here. The intrinsic shapes of the blue LSBGs, whose formation path is not tied to being in a high-density environment, are in particularly good agreement with the inferred shapes of the observational samples, which also sample a wide range of environments.

6. Conclusions

In this work we have presented the first three-dimensional shape inference of the wide-field samples of LSBGs selected in DES, HSC-SSP, and ALFALFA. We find that all three samples are well characterized by oblate spheroids, with minor principal axis ratios (C/A) significantly higher than the thick disks observed in high mass, HSB dwarfs. We also find no significant difference in the shape distribution of red and blue LSBGs, an inference bolstered by the analogous concordance in the distribution of Sérsic indices over red and blue LSBGs.

Our inferred shape distributions are in good agreement with the shape distributions inferred for cluster UDGs (Burkert 2017; Rong et al. 2020). These results suggest that the intrinsic shapes of LSBGs are not greatly affected by their environments. We also find some evidence that LSBGs are unable to maintain stellar disks at stellar masses where normal, HSB dwarfs regularly maintain thick disks. Intriguingly, we do note that there is evidence that these UDGs are still able to support gaseous disks (Mancera Piña et al. 2019b, 2020; Gault et al. 2021). However, more work is needed to address both the mass incompleteness of HSB dwarf samples below $M_\star \sim 10^8 M_\odot$ and the large uncertainties in the distance estimate of the LSBG samples.

The different formation mechanisms proposed by cosmological simulations for UDGs and LSBGs manifest strongly in their intrinsic shape distributions. We find that our results are in some conflict with simulated UDGs that form in high-spin halos and those that are puffed up through vigorous star formation feedback. However, we do find that our observed intrinsic shape distribution is in good agreement with simulated UDGs from the Romulus simulation suite, wherein field UDGs are formed by early major mergers that cause star formation to migrate outward (Wright et al. 2021) and cluster UDGs are formed via environmental quenching and tidal heating (Tremmel et al. 2020).

These results show that intrinsic shape distributions are able to provide promising constraints on the formation path of the extreme LSB end of the dwarf galaxy population. The results in this work suggest that the intrinsic shapes of the LSB and HSB galaxy populations may begin to converge at low masses. However, future observational efforts to contextualize the LSBG population face two substantial technical challenges: linking LSBG and HSB samples in order to systematically characterize dwarf properties across the spectrum of surface brightnesses, and establishing distance measures to LSBGs in the field. Upcoming survey instruments such as the the Legacy Survey of Space and Time (LSST), the Prime Focus Spectrograph Subaru Strategic Program (PFS-SSP), the Dark Energy Spectroscopic Instrument (DESI), the Widefield ASKAP L-band Legacy All-sky Blind surveY (WALLABY), and the Square Kilometer Array (SKA), will provide the necessary sensitivity and survey power to make significant strides in the former. Work on the latter is an ongoing area of development (J. Greco et al, 2021 in preparation), and will allow analyses such as the one presented in this work to provide a truly comprehensive view of the diversity in dwarf structure.

Appendix
Mock Recovery Tests

We extend the mock recovery tests of Kado-Fong et al. (2020b) to include the relation between surface brightness and
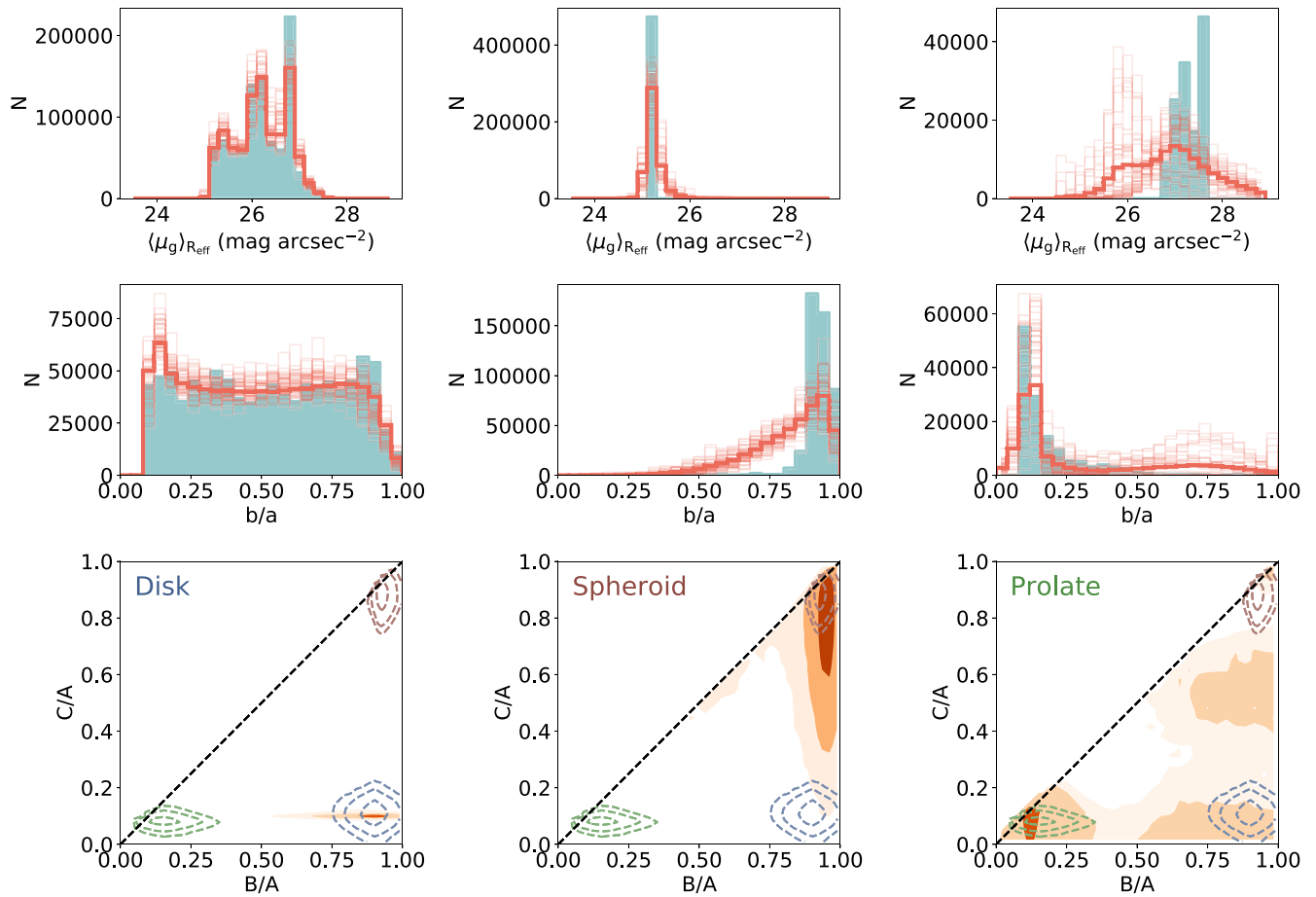
Figure 10. Recovery results for joint inference of the three extreme mock populations presented in Kado-Fong et al. (2020b). Each column shows a different mock population; from left to right, we show the disk, spheroid, and prolate mock populations. *Top row:* the surface brightness distribution for each population. The thick orange curves show our posterior sample (thin orange curves show individual pulls from the posterior). The solid teal histograms show the observed population. *Middle row:* the same for the ellipticity distributions. *Bottom row:* we show the intrinsic axis ratio distribution of the posterior sample as filled orange contours. The analogous results from ellipticity-only inferences are shown by the dashed contours.

intrinsic shape in our mock recovery tests. We implement this relation by computing the expected surface brightness of each synthetic population given the intrinsic shape and viewing angle of each mock galaxy. We do not impose surface brightness limits for these mock tests. Because the mock galaxies projected structural parameters are not remeasured from mock HSC imaging, the absolute value of the surface brightnesses in this test are not consequential to the results. Rather, the test is designed to evaluate our ability to recover the shape of the surface brightness distribution. In Figure 10, we show the inferred intrinsic shape distribution of the posterior sample, as well as the distribution of the model population in

average surface brightness (top row) and ellipticity (middle row). We find that the joint inference, on average, makes the inference more uncertain. However, the inference actually becomes more precise for the disky mock population. This can be understood by considering that the correlation between surface brightness, ellipticity, and viewing angle is maximized for a disky object. The inference becomes more precise due to the additional information provided by this covariance. For the spheroidal and prolate populations, however, the surface brightness distributions are very narrow. Thus, although two extra parameters must now be fitted, the surface brightness provides relatively little extra information.

ORCID iDs

Erin Kado-Fong ⓘ https://orcid.org/0000-0002-0332-177X
Majid Mohammad ⓘ https://orcid.org/0000-0001-9125-3297
Johnny Greco ⓘ https://orcid.org/0000-0003-4970-2874
Jenny E. Greene ⓘ https://orcid.org/0000-0002-5612-3427
Elizabeth A. K. Adams ⓘ https://orcid.org/0000-0002-9798-5111
Song Huang ⓘ https://orcid.org/0000-0003-1385-7591
Lukas Leisman ⓘ https://orcid.org/0000-0001-8849-7987
Ferah Munshi ⓘ https://orcid.org/0000-0002-9581-0297

References

Aihara, H., AlSayyad, Y., Ando, M., et al. 2019, PASJ, 71, 114
Alabi, A. B., Romanowsky, A. J., Forbes, D. A., Brodie, J. P., & Okabe, N. 2020, MNRAS, 496, 3182
Amorisco, N. C., & Loeb, A. 2016, MNRAS, 459, L51
Baldry, I. K., Driver, S. P., Loveday, J., et al. 2012, MNRAS, 421, 621
Barbary, K. 2016, JOSS, 1, 58
Barbosa, C. E., Zaritsky, D., Donnerstein, R., et al. 2020, ApJS, 247, 46
Bell, E. F., McIntosh, D. H., Katz, N., & Weinberg, M. D. 2003, ApJS, 149, 289
Bosch, J., Armstrong, R., Bickerton, S., et al. 2018, PASJ, 70, S5
Burkert, A. 2017, ApJ, 838, 93
Cardona-Barrero, S., Di Cintio, A., Brook, C. B. A., et al. 2020, MNRAS, 497, 4282
Carlsten, S. G., Greene, J. E., Greco, J. P., Beaton, R. L., & Kado-Fong, E. 2021, arXiv:2105.03435
Chan, T. K., Kereš, D., Wetzel, A., et al. 2018, MNRAS, 478, 906
Costantin, L., Méndez-Abreu, J., Corsini, E. M., et al. 2018, A&A, 609, A132
Dalcanton, J. J., Spergel, D. N., Gunn, J. E., Schmidt, M., & Schneider, D. P. 1997, AJ, 114, 635
Danieli, S., & van Dokkum, P. 2019, ApJ, 875, 155
Danieli, S., van Dokkum, P., & Conroy, C. 2018, ApJ, 856, 69
Dey, A., Schlegel, D. J., Lang, D., et al. 2019, AJ, 157, 168
Di Cintio, A., Brook, C. B., Dutton, A. A., et al. 2017, MNRAS, 466, L1
Erwin, P. 2015, ApJ, 799, 226
Foreman-Mackey, D., Hogg, D. W., Lang, D., & Goodman, J. 2013, PASP, 125, 306
Gault, L., Leisman, L., Adams, E. A. K., et al. 2021, ApJ, 909, 19
Giovanelli, R., Haynes, M. P., Kent, B. R., et al. 2005, AJ, 130, 2598
Greco, J. P. 2018, PhD thesis, Princeton Univ.
Greco, J. P., Greene, J. E., Strauss, M. A., et al. 2018, ApJ, 857, 104
Haynes, M. P., Giovanelli, R., Martin, A. M., et al. 2011, AJ, 142, 170
Huang, S., Leauthaud, A., Greene, J. E., et al. 2018, MNRAS, 475, 3348

Janowiecki, S., Jones, M. G., Leisman, L., & Webb, A. 2019, MNRAS, 490, 566
Jiang, F., Dekel, A., Freundlich, J., et al. 2019, MNRAS, 487, 5272
Kado-Fong, E., Greene, J. E., Greco, J. P., et al. 2020a, AJ, 159, 103
Kado-Fong, E., Greene, J. E., Hendel, D., et al. 2018, ApJ, 866, 103
Kado-Fong, E., Greene, J. E., Huang, S., et al. 2020b, ApJ, 900, 163
Lee, M. G., Kang, J., Lee, J. H., & Jang, I. S. 2017, ApJ, 844, 157
Leisman, L., Haynes, M. P., Janowiecki, S., et al. 2017, ApJ, 842, 133
Liao, S., Gao, L., Frenk, C. S., et al. 2019, MNRAS, 490, 5182
Mancera Piña, P. E., Aguerri, J. A. L., Peletier, R. F., et al. 2019a, MNRAS, 485, 1036
Mancera Piña, P. E., Fraternali, F., Adams, E. A. K., et al. 2019b, ApJL, 883, L33
Mancera Piña, P. E., Fraternali, F., Oman, K. A., et al. 2020, MNRAS, 495, 3636
Martínez-Delgado, D., Läsker, R., Sharina, M., et al. 2016, AJ, 151, 96
McGaugh, S. S., Bothun, G. D., & Schombert, J. M. 1995, AJ, 110, 573
Méndez-Abreu, J., Costantin, L., Aguerri, J. A. L., de Lorenzo-Cáceres, A., & Corsini, E. M. 2018, MNRAS, 479, 4172
Munshi, F., Brooks, A., Applebaum, E., et al. 2021, arXiv:2101.05822
Muzzin, A., Marchesini, D., Stefanon, M., et al. 2013, ApJS, 206, 8
Padilla, N. D., & Strauss, M. A. 2008, MNRAS, 388, 1321
Peng, C. Y., Ho, L. C., Impey, C. D., & Rix, H.-W. 2010, AJ, 139, 2097
Prole, D. J., van der Burg, R. F. J., Hilker, M., & Spitler, L. R. 2021, MNRAS, 500, 2049
Prugniel, P., & Simien, F. 1997, A&A, 321, 111
Román, J., Beasley, M. A., Ruiz-Lara, T., & Valls-Gabaud, D. 2019, MNRAS, 486, 823
Román, J., & Trujillo, I. 2017a, MNRAS, 468, 703
Román, J., & Trujillo, I. 2017b, MNRAS, 468, 4039
Rong, Y., Dong, X.-Y., Puzia, T. H., et al. 2020, ApJ, 899, 78
Rong, Y., Guo, Q., Gao, L., et al. 2017, MNRAS, 470, 4231
Sánchez-Janssen, R., Méndez-Abreu, J., & Aguerri, J. A. L. 2010, MNRAS, 406, L65
Sandage, A., & Binggeli, B. 1984, AJ, 89, 919
Sevilla-Noarbe, I., Bechtol, K., Carrasco Kind, M., et al. 2021, ApJS, 254, 24
Simonneau, E., Varela, A. M., & Munoz-Tunon, C. 1998, NCimB, 113B, 927
Tanoglidis, D., Drlica-Wagner, A., Wei, K., et al. 2021, ApJS, 252, 18
Tremmel, M., Karcher, M., Governato, F., et al. 2017, MNRAS, 470, 1121
Tremmel, M., Quinn, T. R., Ricarte, A., et al. 2019, MNRAS, 483, 3336
Tremmel, M., Wright, A. C., Brooks, A. M., et al. 2020, MNRAS, 497, 2786
van der Burg, R. F. J., Muzzin, A., & Hoekstra, H. 2016, A&A, 590, A20
van Dokkum, P. G., Abraham, R., Merritt, A., et al. 2015, ApJL, 798, L45
Van Nest, J. D., Munshi, F., Wright, A. C., et al. 2021, arXiv:2108.12985
Wang, W., Han, J., Sonnenfeld, A., et al. 2019, MNRAS, 487, 1580
Wright, A. C., Tremmel, M., Brooks, A. M., et al. 2021, MNRAS, 502, 5370
Yagi, M., Koda, J., Komiyama, Y., & Yamanoi, H. 2016, ApJS, 225, 11
York, D. G., Adelman, J. A., John, E. J., et al. 2000, AJ, 120, 1579
Zaritsky, D., Donnerstein, R., Dey, A., et al. 2019, ApJS, 240, 1